https://doi.org/10.5194/egusphere-2026-5053
Preprint. Discussion started: 7 September 2026

WAVEGUISE - Wavefield Analysis and Segmentation unraveling an interpretable Set of Wave Packets

Robert Reichert[1,2], Pierre-Dominique Pautet[3], and Martina Bramberger[4]

[1]Deutsches Zentrum für Luft- und Raumfahrt, Institut für Physik der Atmosphäre, Wessling, Germany
[2]Meteorological Institute Munich, Ludwig-Maximilians-Universität, Munich, Germany
[3]Center for Atmospheric and Space Sciences/Physics Department, State University, Logan, UT, USA
[4]National Center for Atmospheric Research, Boulder, CO, USA

Correspondence: Robert Reichert (robert.reichert@dlr.de)

Abstract. Atmospheric waves are never perfectly monochromatic and show modulations in amplitude, wavelength, and frequency due to transient background conditions. In observations, they often appear as complex superpositions of multiple interacting wave components. To disentangle this superposition into individual interpretable wave packets and to study their instantaneous spectral properties in an automatic fashion, we introduce a new method: the Wavefield Analysis and Segmentation unraveling an interpretable set of wave packets (WAVEGUISE). Based on the continuous wavelet transform, WAVEGUISE combines watershed segmentation from image processing and density based spatial clustering algorithms to partition the wavelet domain into coherent regions of shared temporal, spatial, and spectral characteristics. We demonstrate the method using three observational data sets of increasing dimensionality: a) a 25-day pressure time series (1-D) from a long-duration super-pressure balloon obtained during the Strateole-2 campaign, b) a $1,400 \times 500\,\mathrm{km}$ Q-line radiance swath (2-D) from the Atmospheric Waves Experiment (AWE), and c) a OH (3,1) band intensity video sequence (3-D) from the Advanced Mesospheric Temperature Mapper. Applied to these data sets, WAVEGUISE acts as a magnifying glass. The segmentation into a set of dominant and subdominant interpretable wave packets reveals a significantly enhanced level of detail enabling to precisely study dynamical processes such as e.g. wave-wave interaction and to improve wave statistics.

1 Introduction

Atmospheric observations often reveal a superposition of periodic oscillations arising, for example, from planetary waves, tides, gravity waves (GW), and the products of their turbulent breakdown. The spatial scales of these oscillations span a broad range, from 10^0 to 10^4 km, and their periods range from minutes to weeks (Fritts and Alexander, 2003). Because the atmospheric background state is transient, wave amplitudes are modulated and their spectral characteristics may vary in space and time. This variability is further enhanced by wave–wave interactions. Consequently, atmospheric waves are never monochromatic in practice and are more appropriately described as wave packets localized in space, time, wavenumber, and frequency. The spectral analysis of atmospheric waves therefore requires a tool that can determine their spectral properties as functions of space and time, i.e. instantaneous frequencies and wavenumbers. In this work, we employ the continuous wavelet transform (CWT) (Torrence and Compo, 1998; Ungermann and Reichert, 2025). The CWT is widely used in the geophysical community for time–frequency analysis of one-dimensional (1-D) data sets, including lidar temperature measurements, airglow observations,

https://doi.org/10.5194/egusphere-2026-5053
Preprint. Discussion started: 7 September 2026

radiosonde profiles, long-duration balloon measurements, and satellite observations (Chane-Ming et al., 2000; Hertzog and Vial, 2001; Vial et al., 2001; Rauthe et al., 2006; Werner et al., 2007; Wright and Gille, 2013; Ehard et al., 2016; Baumgarten et al., 2017; Reichert et al., 2019; Wing et al., 2021; Gisinger et al., 2022; Reichert et al., 2024; Giongo et al., 2025; Kaifler et al., 2025). In two dimensions (2-D), the CWT has been applied to lidar temperature measurements and airglow observations (Kaifler et al., 2017; Chen and Chu, 2017; Geldenhuys et al., 2022; Reichert et al., 2026), while the related 2-D S-transform (ST) has been applied, for example, to AIRS temperature measurements (e.g. Hindley et al., 2016). In three dimensions (3-D), applications have so far largely been limited to the 3-D ST, for example for AIRS temperature measurements (Wright et al., 2017; Hindley et al., 2019; Berthelemy et al., 2025), whereas a 3-D implementation of the CWT has only recently become publicly available (Ungermann and Reichert, 2025). For completeness, we acknowledge the S3D method, which is another 3-D spectral-analysis technique based on running least-squares harmonic fits that account for spatial variability in spectral components (e.g. Lehmann et al., 2012; Krisch et al., 2017; Strube et al., 2021).

In 2-D and 3-D, in order to reduce the amount of required disk space, spectra have been collapsed to study only the dominant wave components (e.g. Hindley et al., 2016; Reichert et al., 2026). In other words, overlapping waves have been neglected so far. Only in 1-D applications a few studies have attempted to take all present wave modes into account. When lower-amplitude waves were included in the analysis, Wright and Gille (2013) reported, on average, 68 % larger GW momentum fluxes in the lower stratosphere in May 2006 based on satellite measurements. Since the vertical transport of horizontal pseudo-momentum, hereafter referred to as momentum flux, depends on wave amplitude squared, wavelength, and frequency (Ern et al., 2004), many studies focus primarily on dominant wave modes, i.e. on the most prominent wave signatures identified in the analyzed spectra or fields, often without systematically accounting for weaker-amplitude contributions across the full resolved spectrum. Kaifler et al. (2025) concluded that *"small-scale waves with weak temperature amplitudes may make a significant contribution to the total momentum flux"*. These findings highlight the importance of analyzing not only dominant but also sub-dominant wave signatures in atmospheric observations in order to obtain a more complete momentum flux distribution. Moreover, tracking the instantaneous spectral properties of these sub-dominant features enables not only more accurate estimates of momentum fluxes and wave drag but also supports a more detailed interpretation of wave–mean-flow and wave–wave interactions. In this work, we present WAVEGUISE, an algorithm that decomposes a superposition of waves into individual, coherent, and physically interpretable wave packets in data sets of up to three dimensions. The manuscript is structured as follows. First, we provide an overview of the methodology, including data pre-processing, the CWT, denoising, segmentation, filtering, clustering, reconstruction, and the retrieval of spectral properties. In Sect. 3, we apply WAVEGUISE to three observational data sets of increasing dimensionality. The main findings are summarized in Sect. 4.

2 Methods

The wavefield analysis is based on the CWT, implemented for up to three dimensions in the *JuWavelet* Python package (Ungermann and Reichert, 2025). Segmentation summarizes the key idea which is to identify regions that are associated with a local peaks in wavelet space. This is performed using the watershed algorithm from image processing (van der Walt et al., 2014;

https://doi.org/10.5194/egusphere-2026-5053
Preprint. Discussion started: 7 September 2026

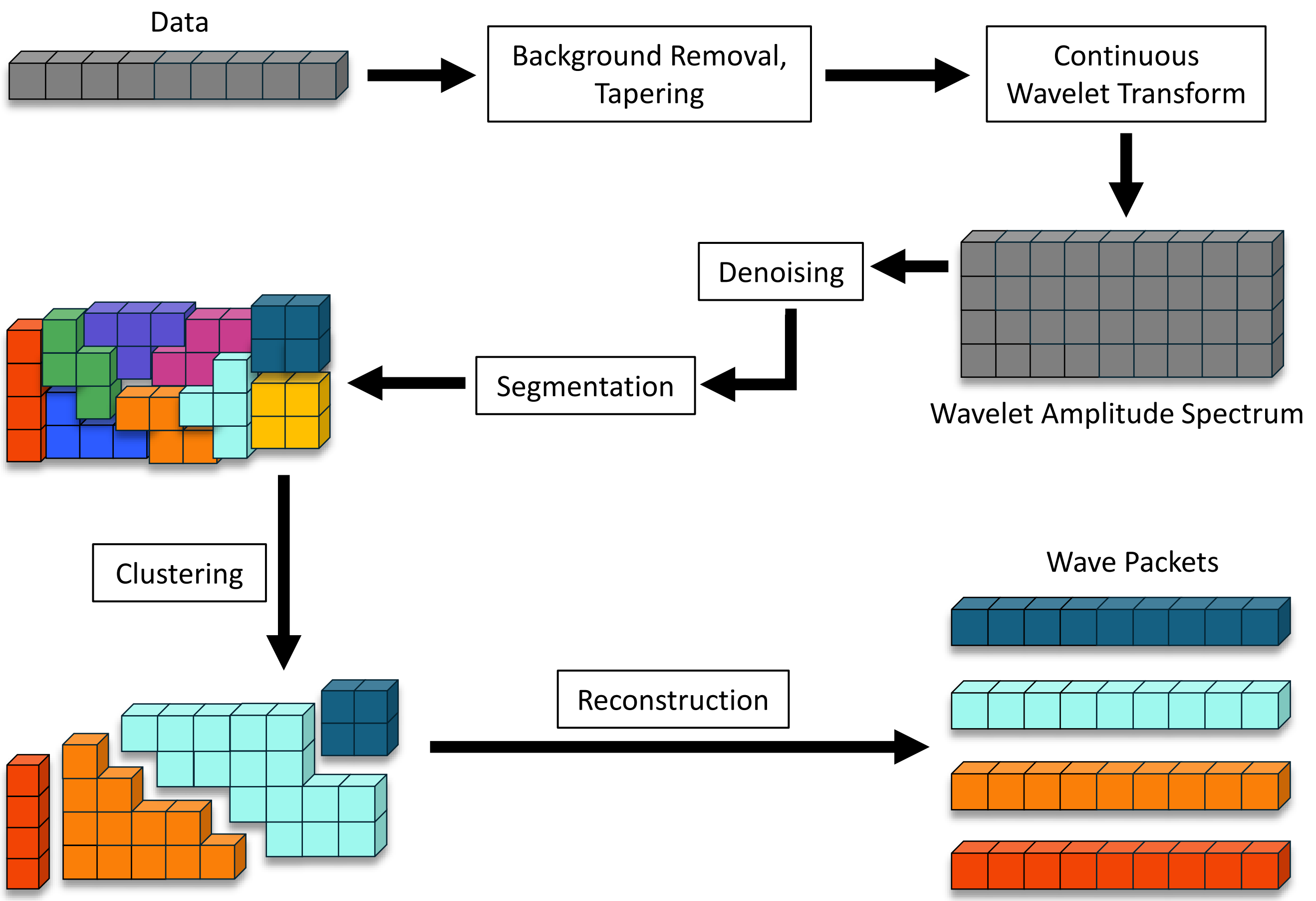

Figure 1. Schematic of the WAVEGUISE algorithm.

Pedregosa et al., 2011). Since the segmentation isolates wave packets based on minima in wavelet space, amplitude modulations can be a reason for an over–segmentation even when spectral properties are identical. Hence, we add a density-based spatial clustering algorithm with noise (DBSCAN) to merge related partitions in the spectral domain (Ester et al., 1996; Pedregosa et al., 2011). In addition, wave packets are only treated as separate when they are disconnected in physical space. The overall workflow is illustrated in Figure 1. In the following, we describe WAVEGUISE step by step, starting with the data preprocessing.

2.1 Background Removal

Observational data sets frequently exhibit low-frequency background variations and non-periodic boundaries. In time-frequency analyses, these characteristics can lead to enhanced spectral power near the data set edges, thereby obscuring or distorting

https://doi.org/10.5194/egusphere-2026-5053
Preprint. Discussion started: 7 September 2026

higher-frequency features of interest. To mitigate these effects, we apply a two-step background removal procedure to separate large-scale variability from small-scale structures. The method is formulated generically and can be applied to one-, two-, or three-dimensional data sets by performing the operations along each dimension. The low-frequency background BG is defined as

$$BG(\mathbf{x}) = P_n(\mathbf{x}) + \sum_m c_m e^{i\mathbf{kx}}$$

where P_n is a polynomial of degree n and c_m are complex-valued Fourier coefficients. First, the data are mean-centered and a linear trend ($n = 1$) is estimated using a least-squares linear fit which is subsequently subtracted from the data. Second, the detrended data are transformed into Fourier space, where the lowest-frequency components ($m \in [0,1]$) are removed. This suppresses remaining large-scale contributions that are not captured by the linear fit and that are usually too large to be reliably identified in wavelet analysis. The filtered signal is then reconstructed by inverse Fourier transform, yielding the high-pass component. This decomposition provides a consistent separation into large-scale background and small-scale variability and is directly extendable to higher dimensions by applying the least-square fit and Fourier filtering along each dimension. Though the background removal technique is not in focus of this work, for completeness we have attached figures showing the defined background for each of the case studies in Appendix A.

2.2 Tapering

To further suppress boundary-related artifacts in the wavelet analysis, the data are smoothly tapered towards the domain boundaries. This is achieved by applying a multidimensional Tukey window, which gradually reduces the signal amplitude to zero near the edges while preserving the central part of the domain. The width of the tapering region is defined as a fraction of the domain size (here 10 %), ensuring that only the outer margins are affected. This approach effectively suppresses artificial discontinuities at the boundaries and reduces spectral leakage in the subsequent wavelet analysis, while minimally distorting the signal in the interior. This step is important for the subsequent segmentation and interpretation of wavelet amplitudes, as it reduces the risk of misidentifying edge-induced artifacts as physically meaningful structures.

2.3 Continuous Wavelet Transform

We use the *JuWavelet* Python module (Ungermann and Reichert, 2025) to compute the CWT of the preprocessed data. The CWT is a time–frequency analysis tool that yields complex-valued wavelet coefficients W as a function of physical and spectral space. Throughout this work, we employ the complex Morlet wavelet with non-dimensional frequency 2π. This choice ensures admissibility and has the convenient property that wavelet scales correspond directly to wavelengths. The set of scales is defined as $s = s_0 2^{d_j j}$, where s_0 denotes the smallest scale (typically at least twice the resolution of the underlying dataset), d_j controls the scale sampling density (usually in the range $\frac{1}{2}$ to $\frac{1}{8}$), and $j \in \mathbb{N}$ (Torrence and Compo, 1998). The largest scale is chosen such that the corresponding maximum period is approximately half the domain size, consistent with the prior removal of background variations on larger scales. In two dimensions, the transform is additionally evaluated over a set of azimuth angles ϑ uniformly distributed between 0 and π, resulting in a directional ambiguity of π. In three dimensions, an additional

https://doi.org/10.5194/egusphere-2026-5053
Preprint. Discussion started: 7 September 2026

set of zenith angles $\varphi \in [0, \pi]$ is introduced. For purely spatial 3-D data, the 3D-CWT provides a local wavenumber spectrum at each point in space, still subject to the π ambiguity due to the absence of temporal information. In contrast, for datasets with two spatial and one temporal dimension, the transform can be interpreted in terms of phase-speed spectra. In all subsequent steps, we use the wavelet amplitude spectrum $|W|$ (WAS) rather than the wavelet power spectrum $|W|^2$ because interpretation is more intuitive since $|W|$ refers to the instantaneous amplitude of the signal.

2.4 Denoising

To suppress noise in the wavelet domain, we apply a two-stage thresholding procedure to the wavelet coefficients. The method operates on the wavelet decomposition W and uses the corresponding WAS as the quantity on which the thresholds are applied. In a first step, an optional robust colored-noise filter is applied separately at each wavelet scale. For each scale, the median WAS is computed over the remaining dimensions, and the spread is estimated using the scaled median absolute deviation, $sMAD(|W|) = 1.4826 \cdot median(|W| - median(|W|))$. The factor 1.4826 makes the estimator consistent with the standard deviation for Gaussian data, while retaining the robustness of the median-based estimate against outliers. The WAS is then normalized as $|W|_{\text{norm}} = \frac{|W| - median(|W|)}{sMAD(|W|)}$ and coefficients with deviations from the median below a defined multiple of the $sMAD(|W|)$ are removed. In this way, only coefficients that stand out sufficiently from the scale-dependent background distribution are retained. Because the normalization is performed independently for each scale, the procedure accounts for the fact that background amplitudes typically vary with scale, as expected for colored-noise-like processes. Such wavelet-domain thresholding is widely used for denoising because it preserves coherent structures more effectively than filtering performed directly in physical space. Instead of using a constant threshold, we account for the scale dependence of wavelet amplitudes of white noise. Specifically, the threshold decreases with increasing scale according to the expected scaling of white-noise amplitudes in wavelet space. All coefficients whose amplitude falls below this scale-dependent threshold are set to zero, i.e. coefficients satisfying $|W(s)| < |W(s)_{\text{white}}|$ are removed. This approach suppresses coefficients that are consistent with small-amplitude, spatially uncorrelated noise while respecting the intrinsic $\frac{1}{\sqrt{s}}$ scaling of white-noise amplitudes.

2.5 Segmentation

The core objective of this step is to identify coherent regions of enhanced wavelet amplitudes in the wavelet domain, which are interpreted as individual wave packets. These regions are separated by minima in the spectrum and can be understood as multidimensional "canyons" between localized maxima. Segmentation is performed using the watershed algorithm as implemented in the *scikit-image* Python package (van der Walt et al., 2014). Since the watershed algorithm identifies catchment basins associated with local minima, the WAS is first inverted according to $|W|_i = max(|W|) - |W|$, such that regions of high wavelet amplitude correspond to basins. Local minima are identified using the *h_minimum* function, which suppresses shallow minima below a specified prominence threshold h. This parameter controls the sensitivity of the segmentation: smaller (larger) values of h result in a larger (smaller) number of detected partitions. In practice, we set h proportional to the estimated noise level to avoid over-segmentation of noise-induced fluctuations. The detected minima serve as markers for the subsequent watershed flooding procedure. The algorithm then assigns a unique label to each connected region, resulting in a segmented

https://doi.org/10.5194/egusphere-2026-5053
Preprint. Discussion started: 7 September 2026

wavelet domain in which each label corresponds to an individual wave packet. Due to the inherent π ambiguity in ϑ and φ, the WAS is treated as periodic in these coordinates. This is achieved by wrapping the WAS along the corresponding dimensions prior to segmentation, ensuring that structures crossing the domain boundaries are correctly identified as single, connected features. While minima in spectral dimensions should act as boundaries between partitions, the same is not obvious for minima in spatial or temporal dimensions since a wave field can be considered coherent even when its amplitude is modulated.

2.6 Clustering

The segmentation step separates the WAS into contiguous regions of elevated amplitude. However, this purely local criterion may split a physically coherent wave packet into multiple segments when its amplitude varies and exhibits local minima. In such cases, the underlying spectral characteristics (e.g., wavelength or frequency) remain unchanged, and the segments should be treated as a single wave packet. An exception arises when the amplitude approaches zero, indicating a true interruption of the signal; in this case, a separation is physically meaningful. To account for this, we introduce a clustering step in wavelet space that groups segments with similar spectral properties. For each segment, we compute $|W|$-weighted averages of its spectral characteristics. These features are then used as input for a density-based spatial clustering of applications with noise (DBSCAN) (Ester et al., 1996; Pedregosa et al., 2011). DBSCAN groups segments based on their proximity in feature space, controlled by the neighborhood radius ε and the minimum number of points *minPts* required to form a cluster. Throughout this work, we set $minPts = 2$, allowing even the smallest groups of segments to be considered as clusters. Segments classified as noise are retained, as they typically correspond to wave packets with distinct spectral properties rather than spurious detections. In a final step, we examine each cluster in the physical domain (time or space). Segments that belong to the same cluster but are not connected are treated as independent wave packets. Conversely, connected segments within a cluster are merged, effectively reconstructing wave packets with continuous but potentially modulated amplitudes.

2.7 Wave Packet Reconstruction and Spectral Properties

As a result of the segmentation and clustering we obtain unique labels that group wavelet coefficients in the wavelet domain into individual partitions that represent wave packets in physical space. We use these labels to reconstruct each wave packet following Ungermann and Reichert (2025) and to compute their instantaneous spectral properties.

3 Results and Discussion

WAVEGUISE is applied in the following to three observational data sets of increasing dimensionality, where the 1-D example is a pressure timeseries, the 2-D example is a space-borne radiance measurement, and the 3-D example is a video sequence of infrared emission from the OH layer (~ 86 km). Each time, we reconstruct wave packets as identified by WAVEGUISE and determine their instantaneous spectral properties.

https://doi.org/10.5194/egusphere-2026-5053
Preprint. Discussion started: 7 September 2026

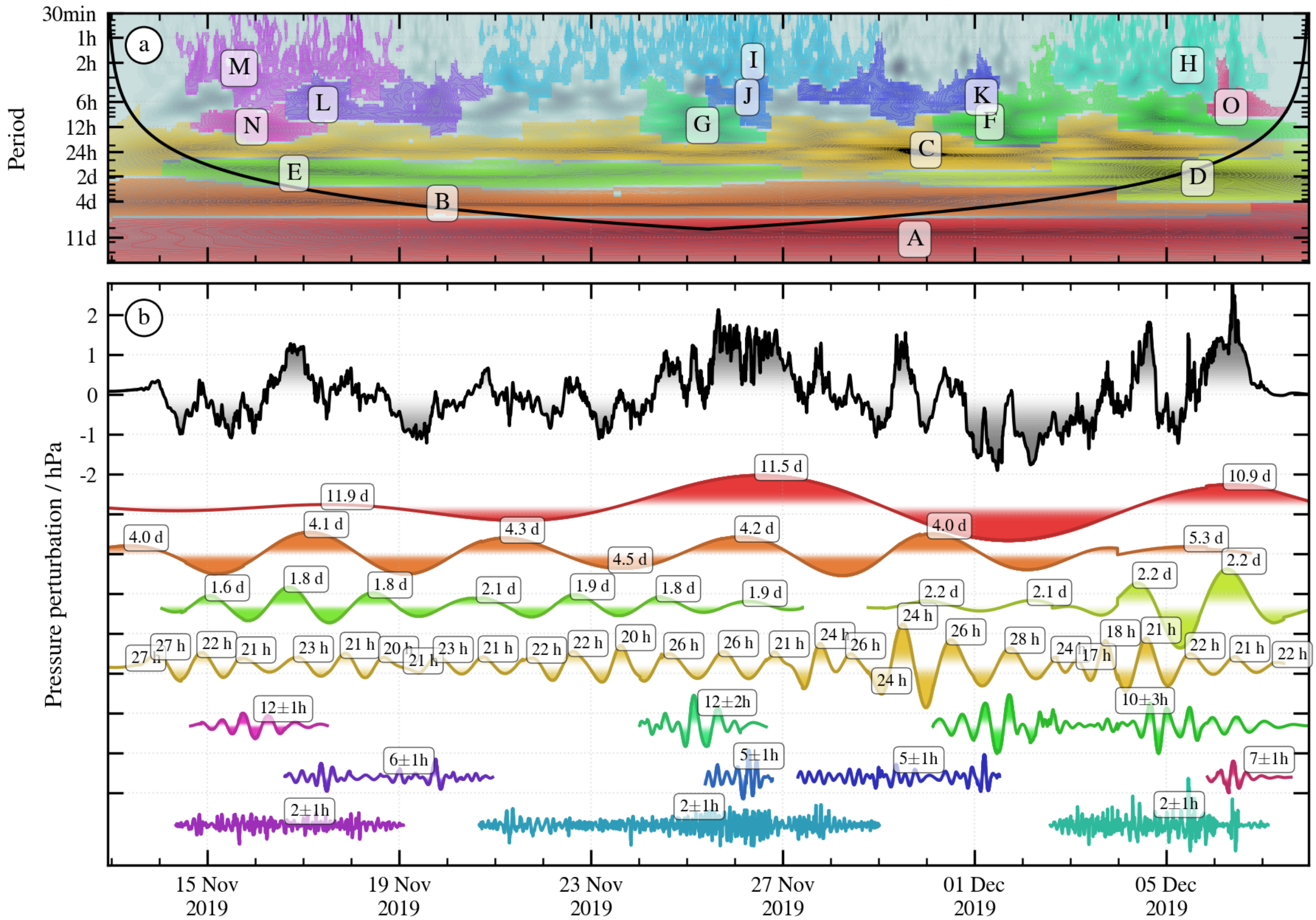

Figure 2. Decomposition of the pressure perturbation measured by a super-pressure long-duration balloon during the Strateole-2 campaign. (a) Wavelet amplitude spectrum as a function of time and period. Colors indicate the individual wave packets identified by WAVEGUISE and labelled A–O. The black curve denotes the cone of influence, outside of which wavelet coefficients are increasingly affected by edge effects. (b) Original pressure perturbation (black) and reconstructed pressure signals of the individual wave packets, vertically offset for clarity and colored according to their corresponding regions in panel (a). Labels indicate the characteristic period of each reconstructed wave packet; standard deviations are given where periods become shorter than 12 h.

https://doi.org/10.5194/egusphere-2026-5053
Preprint. Discussion started: 7 September 2026

3.1 1-D long-duration super-pressure balloon measurements

The Strateole-2 campaign (2019–2022) deployed a fleet of long-duration super-pressure balloons in the tropical lower stratosphere to perform quasi-Lagrangian measurements of atmospheric variables such as temperature, wind, water vapor, and pressure, with a particular focus on GWs and small-scale transport processes (Haase et al., 2018). By drifting for months on constant-density surfaces, the balloons provided in situ observations of tropical stratospheric circulation and wave activity, improving our understanding of processes governing the Brewer–Dobson circulation and stratosphere–troposphere exchange (Corcos et al., 2021; Bramberger et al., 2022; Cao et al., 2022; Corcos et al., 2025).

In this section, we apply WAVEGUISE to a 25-day pressure time series measured by a super-pressure balloon drifting eastward from the Seychelles across Indonesia, Papua New Guinea, and the Solomon Islands. The detrended, tapered, and denoised signal is shown in Fig. 2b, while the corresponding WAS (Fig. 2a) is computed from the detrended and tapered, but not yet denoised, time series. For completeness, the original pressure record, as well as the defined background and noise components, are provided in Appendix A1 as well as a table listing data properties and WAVEGUISE settings. Using a segmentation and clustering approach with 99 % retained variance, 15 superimposed wave packets are identified, each with distinct temporal localization and spectral characteristics (see Fig. 2a (A-O)). The lowest-frequency component (wave packet A) exhibits periods between 10.9 and 11.9 days and is interpreted as an 11-day planetary wave (Salby, 1981; Hirota and Hirooka, 1984). Although this signal lies largely within the COI, and is therefore subject to amplitude underestimation, its reconstruction closely matches the original time series. Wave packet B, with periods of 4.0–5.3 days, is consistent with a 4-day planetary wave. Its reduced amplitude near the beginning and end of the record is partly attributable to COI effects. Notably, the attenuation toward the end coincides with an increase in the amplitude of a quasi-2-day component (wave packet D), suggesting a possible interaction between these modes. Wave packets D and E, with periods between 1.6 and 2.2 days, are consistent with the quasi-2-day wave. A temporary drop below the noise threshold around 28 November 2019 causes this signal to split into two distinct packets. Wave packet C represents a coherent diurnal tidal structure, despite moderate variability in amplitude and period which could result from interference with low-frequency GW modes. Notably, its amplitude peaks during a phase of reduced quasi-2-day wave activity, indicating a potential modulation between these modes. The 11-day, 4-day, 2-day, and diurnal oscillations correspond to planetary-scale atmospheric modes and appear in the balloon record at almost all times. In contrast, higher-frequency components occur intermittently. Wave packets F-O exhibit periods between 2 and 12 hours. Their short periods and temporal localization suggest that these features represent GW packets.

Restricting the reconstruction to the dominant wave mode (not shown) at each time step yields a time series that retains 21 % of the total variance of the analyzed signal, highlighting the importance of multi-component superposition. Overall, the application of WAVEGUISE to a single 25-day pressure time series from a Strateole-2 balloon enables an automatic and physically interpretable decomposition into wave packets, including their temporal localization and spectral properties (amplitude, period, and phase). Without relying on band-pass filtering, the intrinsic atmospheric oscillations emerge naturally, and their complex superposition is disentangled.

https://doi.org/10.5194/egusphere-2026-5053
Preprint. Discussion started: 7 September 2026

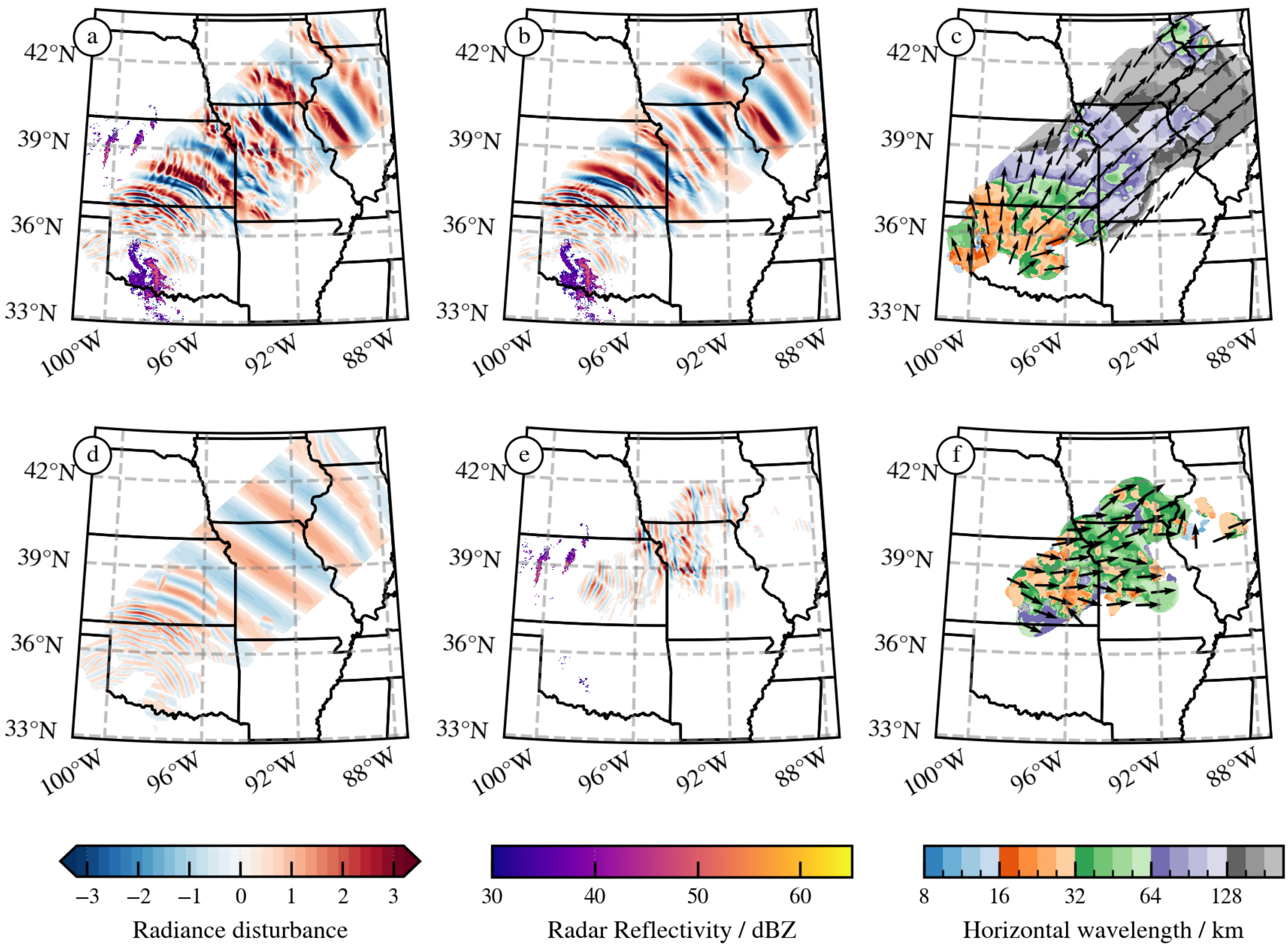

Figure 3. Detrended, denoised, and tapered AWE Q-line radiance swath from orbit 2514 on the 2nd May 2024 ∼06 UTC over the US and NEXRAD radar reflectivity from Dodge City, KS, and Oklahoma City, OK (a). Illustrated are reconstructions of dominant wave modes only (d), convective GW I (b), and convective GW II (e) as well as associated instantaneous wavelengths for convective GW I (c) and convective GW II (f). Arrows indicate the propagation direction.

3.2 2-D AWE Q-line radiance map

The Atmospheric Waves Experiment (AWE), a NASA mission aboard the International Space Station, observes infrared airglow from the OH layer to detect atmospheric GWs in the mesosphere and lower thermosphere (MLT) (Lamborn et al., 2024).
190 Figure 3a shows the detrended, tapered, and denoised band intensity swath of the OH (2,0) band line (hereafter "Q-line") over the United States on 2 May 2024 at about 06 UTC. For completeness, the original Q-line swath, as well as the defined background and noise components, are provided in Appendix A2. A reconstruction of dominant wave modes only (Fig. 3d) captures the main structures: wavelengths increase from southwest to northeast, accompanied by a corresponding change in phase-line

https://doi.org/10.5194/egusphere-2026-5053
Preprint. Discussion started: 7 September 2026

curvature consistent with theory (Vadas and Azeem, 2021). These characteristics are consistent with GWs generated by a convective system over Texas/Oklahoma (see radar reflectivity in Fig. 3ab). Applying WAVEGUISE, however, reveals a more complete picture. Using the settings listed in table A1 we find a total of 14 wave packets that we sort manually. The wave field depicted in Fig. 3b closely resembles the dominant-mode reconstruction and can be attributed to the Texas/Oklahoma source. In contrast, the wave field illustrated in Fig. 3e exhibits systematically smaller spatial scales and phase-line geometries that indicate a distinct source region over Kansas. This interpretation is supported by contemporaneous radar reflectivity observations taken from the NEXRAD weather radar network, which show a large convective system at the Texas–Oklahoma border and additional smaller convective cells in northern Kansas. Similar cases were studied by Yue et al. (2013) and Fritts et al. (2026). While an analysis limited to dominant wave modes would capture only the primary source, it would miss the weaker, yet physically meaningful contributions. By resolving both dominant and subdominant wave components, WAVEGUISE reveals the superposition of multiple convectively generated GW fields, including contributions from west Kansas and north Missouri. This demonstrates that a substantial fraction of the wave field—both in terms of spatial scales and source attribution—remains unresolved when considering dominant modes alone.

3.3 3-D AMTM brightness intensity video

The Advanced Mesospheric Temperature Mapper (AMTM), developed by Utah State University, receives infrared band emissions from the OH-layer at approximately 87 km altitude with spatial and temporal resolutions of 625 m and 35 s, respectively (Pautet et al., 2014). Given the resolution and a field of view (FOV) of 200×160 km, the imager is well suited to detect medium- to small-scale GWs, including mountain waves and secondary GWs, as well as even smaller-scale Kelvin–Helmholtz instabilities (KHI) in the MLT (e.g. Pautet et al., 2021; Mixa et al., 2021; Reichert et al., 2026; Mixa et al., 2026). Snapshots of received band intensity (BI) taken every $\sim$5 min during the night of 16–17 May 2018 at Río Grande, Argentina, are shown in Fig. 4. For completeness, the original band intensity video sequence, as well as the defined background, denoised data, and reconstruction of dominant wave modes only are provided in the Supplement. The observations reveal a superposition of numerous wave-like structures and possible KHI, exhibiting different amplitudes, wavelengths, propagation directions, frequencies, phase speeds, and localizations, thereby illustrating the complexity of the wave field. Applying the 3-D CWT to 155 consecutive BI maps yields a 6-D WAS, $|W|(s,\vartheta,\varphi,x,y,t)$, which requires a substantial amount of disk space. To obtain a compact, memory-efficient representation of this 6-D WAS, we collapse the two spatial dimensions by taking the 95th percentile over the FOV, resulting in a reduced 4-D WAS, $|W|_{95}(s,\vartheta,\varphi,t)$. This procedure emphasizes the upper tail of the wavelet-amplitude distribution and therefore highlights localized regions of enhanced wave activity, while reducing the influence of background variability, noise, and isolated small-scale, large-amplitude outliers. Consequently, the wave field segmentation is performed in spectral–temporal space rather than in the full spectral–spatio-temporal domain.

Figure 5 illustrates, based on two representative snapshots, how WAVEGUISE analyses and segments the 3-D wave field, identifying a set of eight wave packets that we reduce manually to five interpretable wave packets. To summarize the temporal evolution of the spectral properties of the individual wave packets, we compute amplitude-weighted FOV averages of k_x, k_y, and ω, from which we derive wavelength, frequency, orientation, and phase speed (see Fig. 6). The first wave packet (WP-

https://doi.org/10.5194/egusphere-2026-5053
Preprint. Discussion started: 7 September 2026

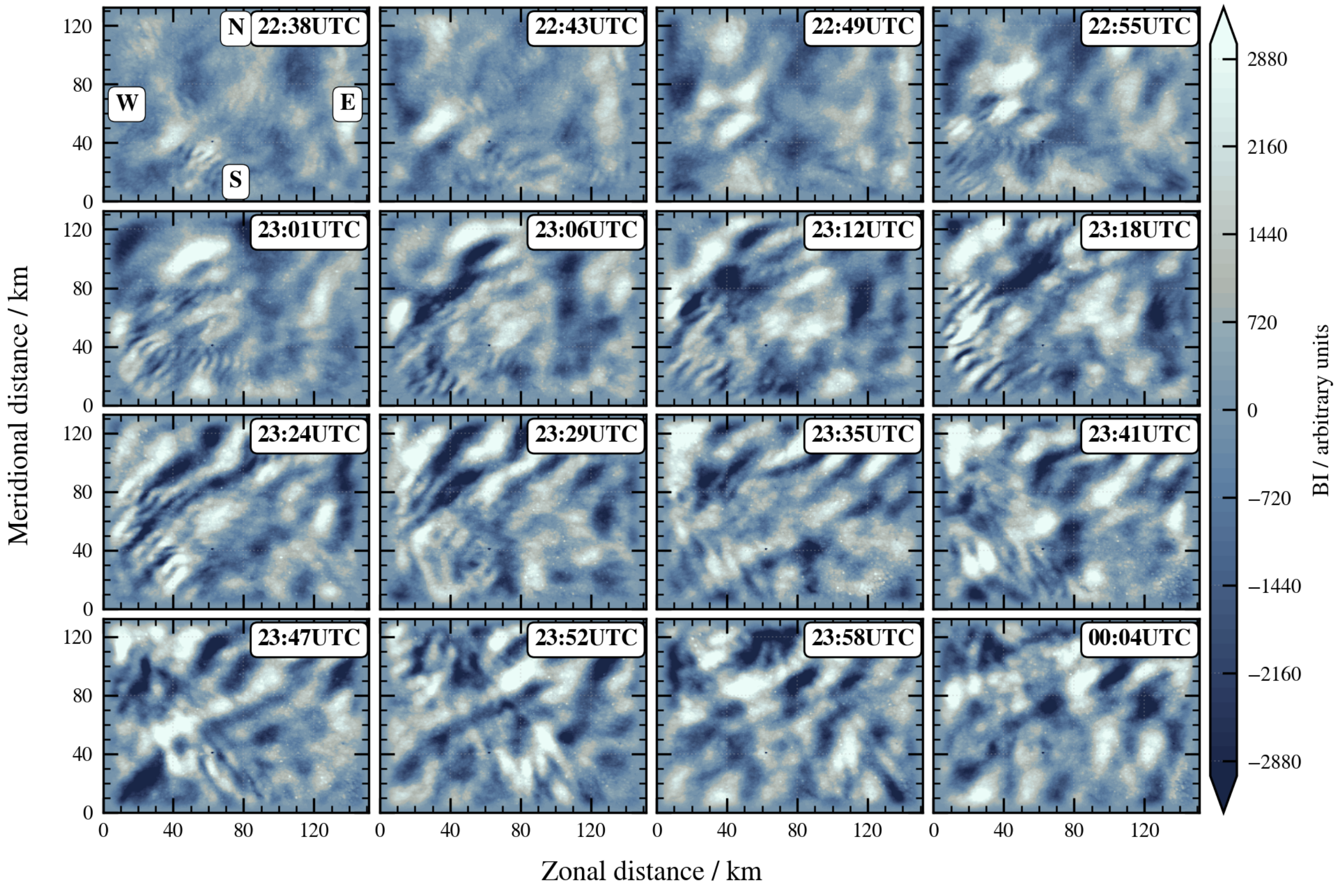

Figure 4. AMTM band intensity measurements every ∼5 min from the night 16-17 May 2018 at Río Grande, Argentina.

I; Fig. 5b,d) extends across the entire FOV and persists throughout the 1.5 h period under analysis. It exhibits the largest amplitudes, has horizontal wavelengths of approximately 25 km, and propagates towards the northwest with a phase speed of about $30\,\mathrm{m\,s^{-1}}$. Even though the spatial structure of WP-I and its coverage of the entire FOV evokes studies of quasi-stationary mountain waves (e.g. Hecht et al., 2018; Mixa et al., 2021; Pautet et al., 2021; Reichert et al., 2026), derived phase speeds of $30\,\mathrm{ms^{-1}}$ very likely exclude an orographic origin. This wave packet dominates the observations throughout the measurement period. Its amplitude approximately doubles within 1.5 h, which may indicate an increase in vertical wavelength and, consequently, reduced phase averaging within the OH layer (Fritts et al., 2014). Alternatively, reduced filtering or damping at lower altitudes could enhance wave amplitudes at MLT heights (Kruse et al., 2016). The second wave packet (WP-II) is localized in the southwestern part of the FOV, shows temporally varying amplitudes, has the smallest scales of approximately 10 km, and migrates eastward with a phase speed of about $30\,\mathrm{m\,s^{-1}}$. We speculate that this wave packet may be attributable to GW-induced KHI (e.g. Mixa et al., 2026). The localization of the KHI appears to be weakly connected to the positive phase of WP-V. The third wave packet (WP-III) has scales similar to WP-II, but propagates much faster, with $c \approx 100\,\mathrm{m\,s^{-1}}$, towards

https://doi.org/10.5194/egusphere-2026-5053
Preprint. Discussion started: 7 September 2026

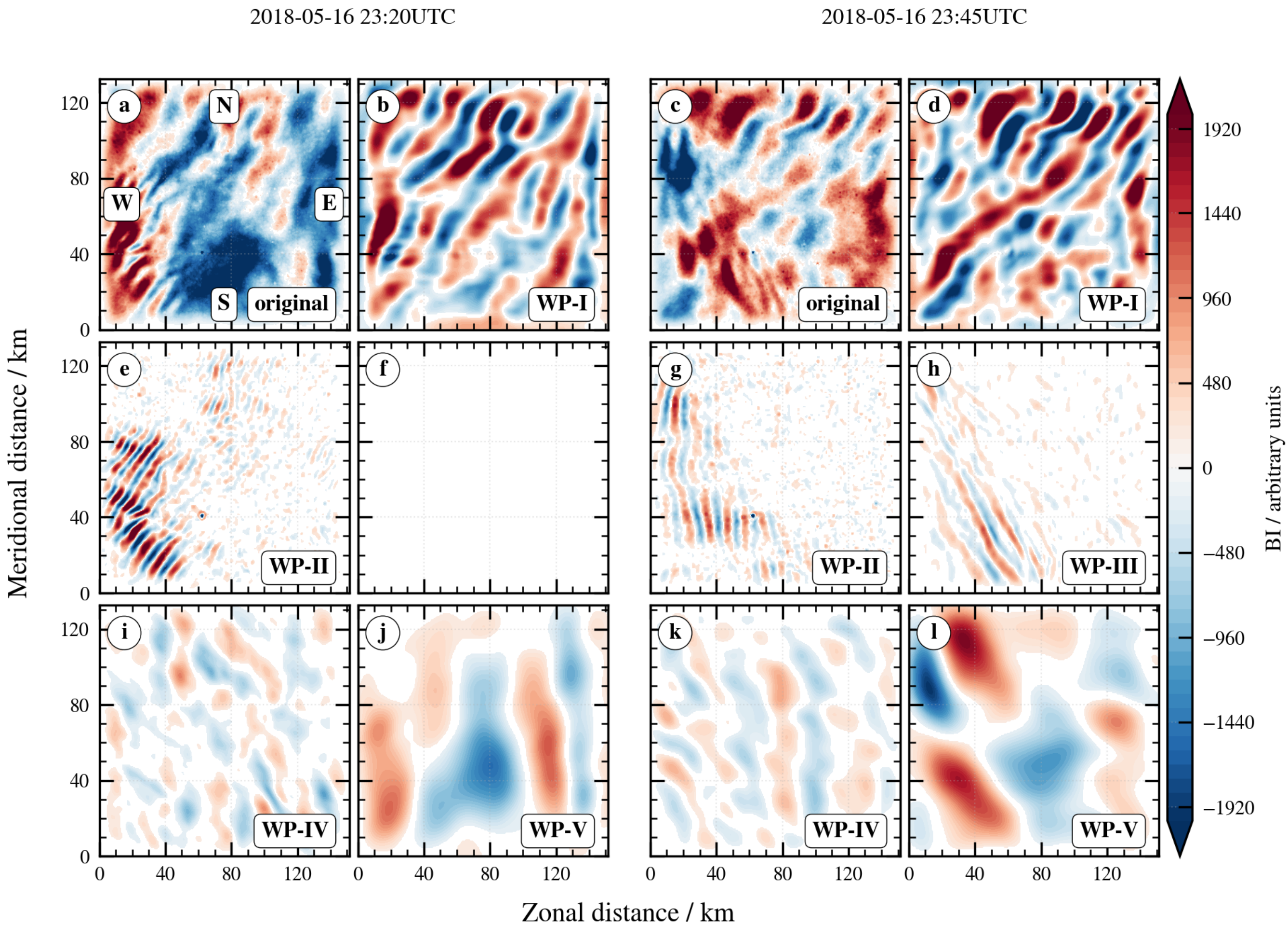

Figure 5. Detrended and tapered BI maps (a,c) and reconstructions of WP-I (b,d), WP-II (e,g), WP-III (h), WP-IV (i,k), and WP-V (j,l). Left panels refer to 2320 UTC and right panels refer to 2345 UTC.

the northeast. In contrast to the other wave packets, WP-III is highly localized (visible for only about 25 min), comprises only about three wave cycles, and clearly enters and exits the FOV. Its observed period of about 1.7 min is notably short for a freely propagating GW in the OH layer. We therefore interpret WP-III as a small-scale, short-lived GW packet whose apparent propagation is likely strongly affected by Doppler shifting by the background wind. The fourth wave packet (WP-IV) is present throughout the FOV, has comparatively small amplitudes, and is characterized by rapid eastward propagation, with $c \approx 100\,\mathrm{m\,s^{-1}}$, and scales of approximately 25 km. It may be associated with secondary GW generation below and upstream of the observational volume (e.g. Vadas et al., 2018; Fritts et al., 2021; Reichert et al., 2026). The fifth wave packet (WP-V) is also present throughout the FOV, exhibits comparatively small amplitudes, has the largest scales of approximately 50 km, and propagates eastward with a phase speed of about $50\,\mathrm{m\,s^{-1}}$.

https://doi.org/10.5194/egusphere-2026-5053
Preprint. Discussion started: 7 September 2026

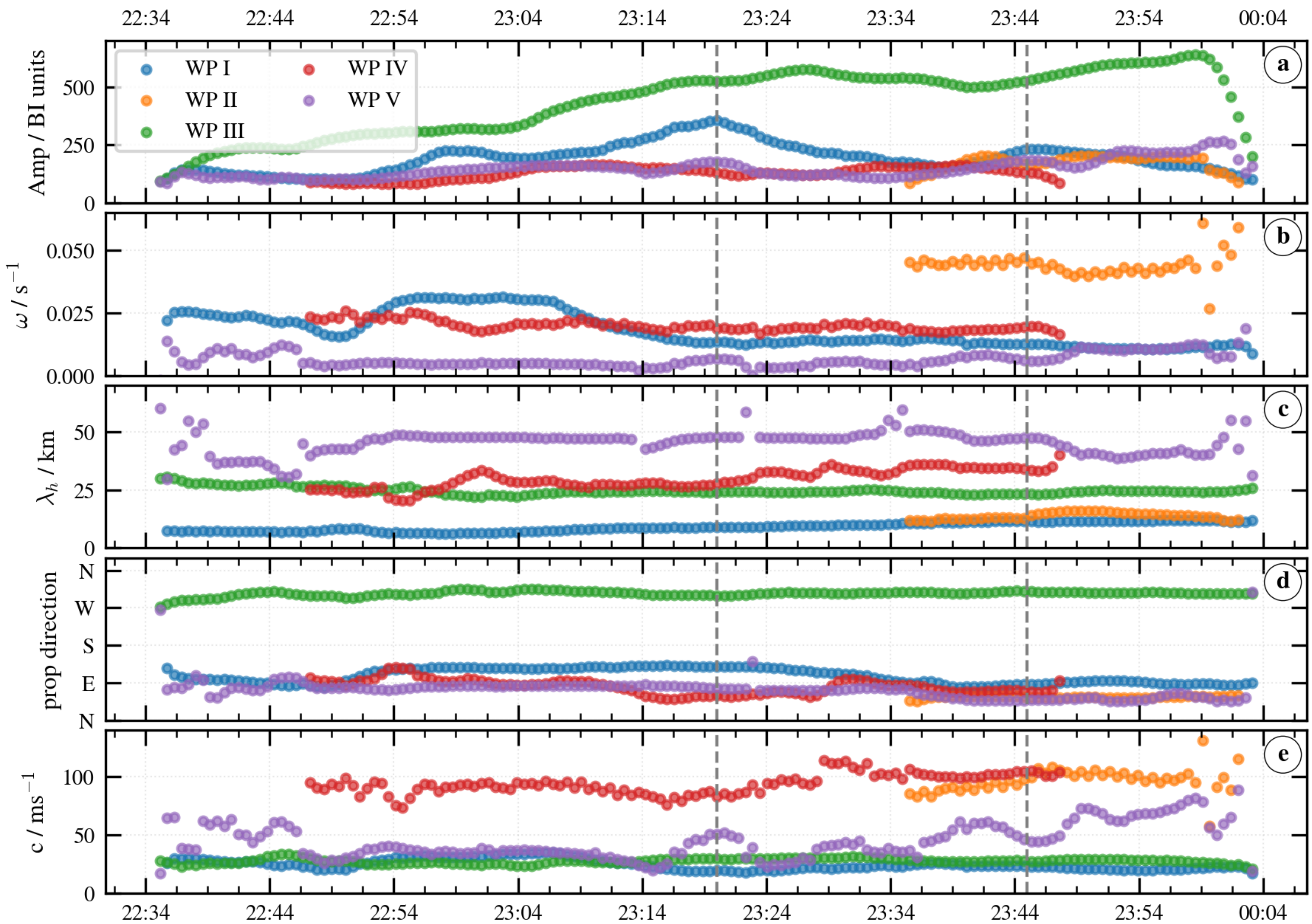

Figure 6. Temporal evolution of FOV-mean parameters amplitudes (a), frequencies (b), wavelengths (c), orientations (d), and phase speeds (e) of wave packets I-V. The two dashed lines indicate the two times at which WP reconstructions are shown in Figure 5.

4 Conclusions

Numerous studies have applied multidimensional CWTs and STs to non-stationary wave fields. However, only a small number of studies have attempted to characterize the full set of simultaneously present wave components, and these approaches have largely been restricted to 1-D applications (Wright and Gille, 2013). In 2-D and 3-D, analyses have typically focused on dominant wave modes, while weaker or subdominant components have received considerably less attention (e.g. Hindley et al., 2016; Reichert et al., 2026). To address this limitation, we introduced the novel WAVEGUISE algorithm as a framework for the analysis, segmentation, and reconstruction of complex wave fields in up to three dimensions. The central objective of WAVEGUISE is to transform the continuous and highly redundant representation obtained from a CWT into a finite set of individually interpretable wave packets, including their spatial or temporal extent and instantaneous spectral properties. The

https://doi.org/10.5194/egusphere-2026-5053
Preprint. Discussion started: 7 September 2026

novelty of WAVEGUISE does not lie in the CWT, watershed segmentation, or clustering individually, but in their combination into a unified workflow for identifying and reconstructing coherent wave packets. In contrast to approaches that characterize a wave field primarily through its dominant spectral components, WAVEGUISE retains subdominant signals and allows multiple wave packets that overlap in physical space and/or time to be distinguished according to their location and extent in wavelet space. WAVEGUISE was designed explicitly for non-monochromatic and evolving wave packets. A single identified packet may therefore exhibit gradual changes in frequency, wavelength, propagation direction, or amplitude while remaining connected in wavelet space. Likewise, spatially curved structures, including circular or ring-like wave patterns, can be identified and reconstructed as individual wave packets. We demonstrated the method using three observational data sets of increasing dimensionality. Despite their fundamentally different sampling geometries, the same methodological concept could be applied to a 1-D pressure time series, a 2-D airglow radiance swath, and a 3-D airglow video sequence. This demonstrates that WAVEGUISE is not restricted to a specific instrument or observational geometry, but provides a general approach for decomposing non-stationary wave fields. We summarize our findings as follows:

– A 25-day long pressure timeseries (1-D) obtained by a super-pressure long-duration balloon during the Strateole-2 campaign was separated into planetary wave packets (observed periods were 11 days, 4 days, and 2 days), a tidal wave component (observed period was 24 h), and GW packets (observed periods ranged from 1 h to 11 h) (see Fig. 2). The juxtaposition of wave packet reconstructions revealed a peak in the 2-day wave amplitude when the 4-day wave vanished and similarly the 2-day wave vanished when the diurnal tide peaked in amplitude. Beyond illustrating the segmentation procedure in wavelet space, this example demonstrates how WAVEGUISE can isolate temporally overlapping spectral components and make their individual evolution directly accessible. Extending this approach to a larger ensemble of balloon observations will enable systematic analyses of wave occurrence, amplitude variability, and spectral characteristics, and provides a framework for investigating potential wave-–wave interactions.

– A Q-line swath (2-D) from the AWE mission showed complex ring-like structures comprising various scales and bended phase lines in the MLT above central US (see Fig. 3). WAVEGUISE identified a dominant ring-like structure emerging from a convective cell located on the border of Oklahoma and Texas. Importantly, analysis of the subdominant packets revealed a second, weaker ring-like structure associated with two smaller convective cells in Kansas. This example highlights a key advantage of the method: physically meaningful wave signatures can be retained and analyzed even when they are masked by stronger components in the full wave field.

– The application of WAVEGUISE to a 1.5 h long AMTM video sequence (3-D) allowed for the separation of wave-like structures differing in wavelength, propagation direction, and phase speed in the MLT above Tierra del Fuego, Argentina (see Fig. 5). The 3-D analysis demonstrates that WAVEGUISE can distinguish structures that overlap not only spatially, but also temporally, and thereby provides a more complete description of the evolving wave field than can be obtained from a single dominant mode or individual image snapshots.

WAVEGUISE contains a number of tunable parameters. In particular, the number and extent of the identified wave packets depend on the assumed noise level, the prominence parameter controlling the partitioning of wavelet space, and the ε neigh-

https://doi.org/10.5194/egusphere-2026-5053
Preprint. Discussion started: 7 September 2026

borhood used during clustering. The number of scales and rotation angles used in the CWT additionally controls the spectral resolution and strongly affects the required computation time and memory. These parameters therefore need to be selected according to the resolution, geometry, and noise characteristics of the observational data set. Once suitable settings have been established for a particular type of observations, however, the same configuration can be applied systematically to larger collections of comparable data. We therefore envision WAVEGUISE not only as a tool for detailed case studies, but also as a basis for constructing statistics of individual wave packets. Such an approach would allow distributions of wave amplitude, wavelength, propagation direction, phase speed, lifetime, and other derived quantities, including momentum flux and wave drag, to be characterized while retaining information about simultaneously occurring and subdominant waves. More generally, the decomposition of complex observations into individual coherent wave packets provides a route toward investigating their sources, evolution, interactions, and dynamical impacts separately. WAVEGUISE thus provides a framework for moving from the description of a complex wave field toward the automated identification, reconstruction, and quantitative analysis of the wave population that constitute it.

Code and data availability. The source code of WAVEGUISE is available on GitHub at https://github.com/Waveguyde/WAVEGUISE. The version used for this study (v1.0.0) is permanently archived on Zenodo at https://doi.org/10.5281/zenodo.22050313.

Appendix A: Data preprocessing and WAVEGUISE settings

The three example data sets analyzed in this study differ substantially in dimensionality, spatial and temporal resolution, domain size, noise characteristics, and spectral content. Consequently, the preprocessing and WAVEGUISE parameters were adapted to the individual data sets. This appendix provides additional details on the preprocessing of each example and summarizes the corresponding WAVEGUISE settings.

A1 1-D pressure time series

Figure A1a shows the original pressure time series obtained from a super-pressure long-duration balloon during the Strateole-2 campaign. To isolate the wave-induced pressure perturbations, a slowly varying background was estimated from a combination of a linear trend and the first Fourier component (see Equ. 2.1). Instrumental noise was represented using the reported pressure uncertainty of $0.1\,\mathrm{hPa}$ (Corcos et al., 2021). The resulting background estimate and noise level are shown in Fig. A1b. The estimated background was subtracted from the original pressure measurements. The remaining perturbation signal was subsequently denoised and tapered over $10\,\%$ of the domain at either boundary to reduce boundary effects in the CWT. The signal used as input to WAVEGUISE is shown in Fig. A1c. The corresponding preprocessing, CWT, and segmentation parameters are summarized in Table A1.

https://doi.org/10.5194/egusphere-2026-5053
Preprint. Discussion started: 7 September 2026

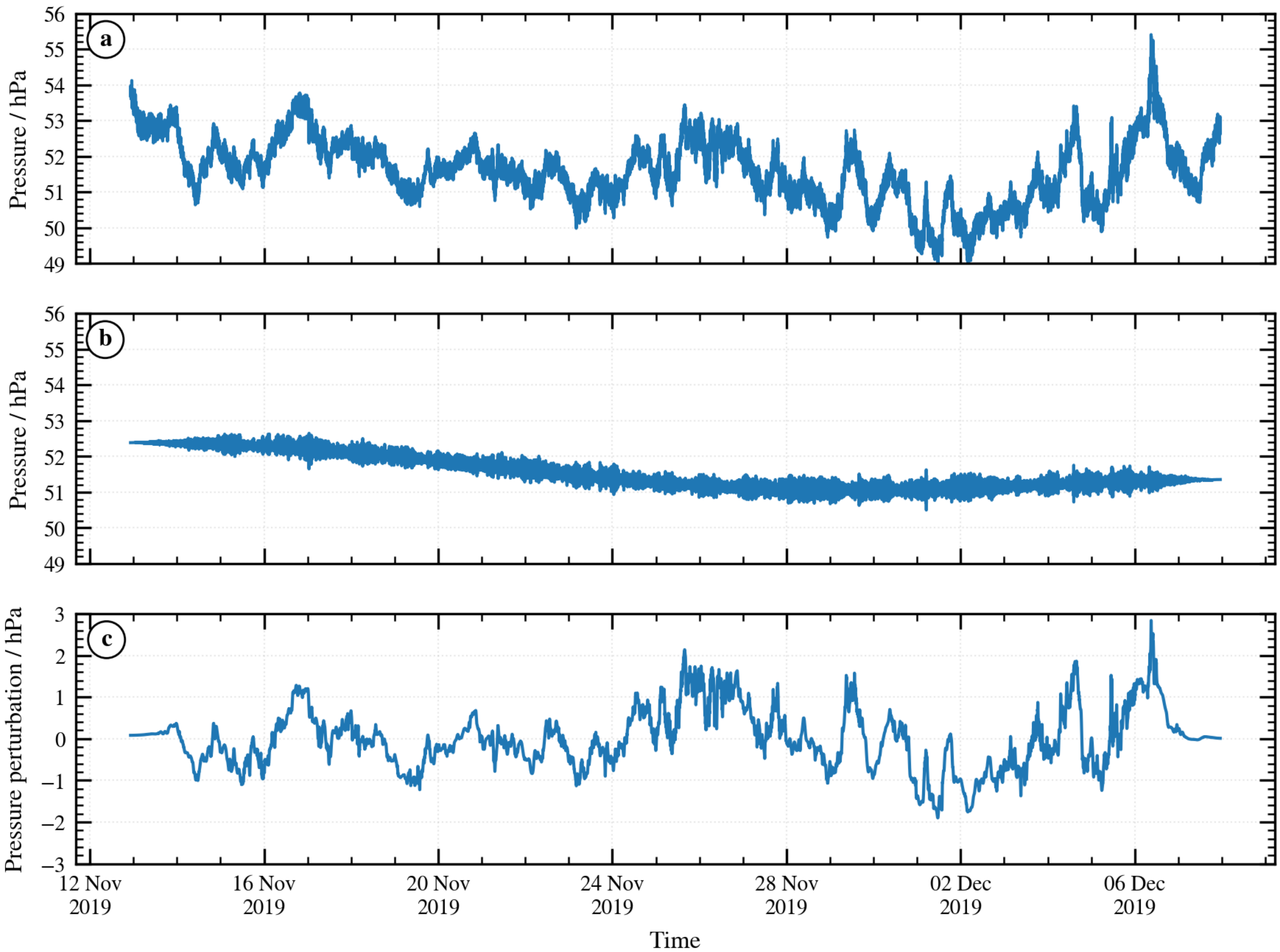

Figure A1. Preprocessing of the 1-D Strateole-2 example. (a) Original pressure time series obtained from a super-pressure long-duration balloon, (b) estimated background and instrumental noise level, and (c) detrended, denoised, and tapered pressure perturbations used as input to WAVEGUISE.

https://doi.org/10.5194/egusphere-2026-5053
Preprint. Discussion started: 7 September 2026

A2 2-D Q-line radiance swath

Figure A2a shows the original Q-line radiance swath observed by AWE on 2 May 2024 at approximately 06:00 UTC. The slowly varying background was estimated from a combination of a linear trend and the first Fourier components (see Equ. 2.1). An instrumental noise level of 0.8 BI units was assumed. The resulting background estimate and noise level are shown in Fig. A2b. After subtraction of the background, the perturbation field was tapered over 10 % of the domain near its boundaries. In addition to the instrument-noise criterion, wavelet coefficients below three times the scale-dependent sMAD were excluded from the subsequent analysis. Figure A2c shows the resulting Q-line radiance perturbation field used for the wavefield analysis. The corresponding WAVEGUISE settings are summarized in Table A1.

https://doi.org/10.5194/egusphere-2026-5053
Preprint. Discussion started: 7 September 2026

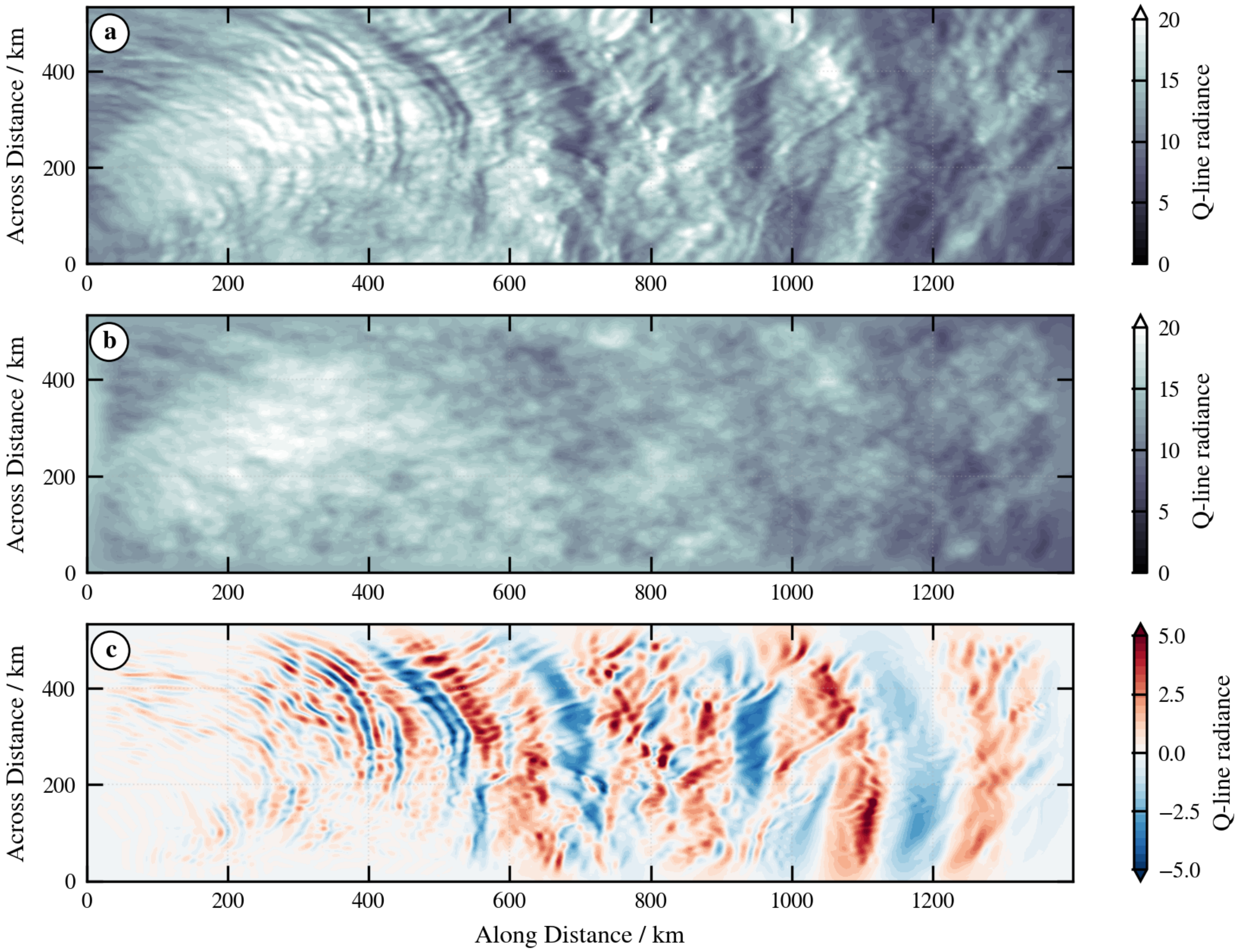

Figure A2. Preprocessing of the 2-D AWE example. (a) Original Q-line radiance swath observed on 2 May 2024 at approximately 06:00 UTC, (b) estimated background and instrumental noise level, and (c) detrended, denoised, and tapered Q-line radiance perturbations used as input to WAVEGUISE.

https://doi.org/10.5194/egusphere-2026-5053
Preprint. Discussion started: 7 September 2026

A3 3-D airglow image sequence

We determine a three-dimensional slowly varying background via a combination of a linear trend and the first Fourier components (see Equ. 2.1). An instrumental noise level of 80 BI units was assumed. After subtraction of the background, the perturbation field was tapered over 10 % of the domain near its boundaries. In the process of saving memory space, we compute the 95th percentile of the WAS along the spatial dimensions which results in an effective noise reduction such that we include no additional denoising step. The resulting three-dimensional perturbation field is subsequently analyzed using the 3-D implementation of WAVEGUISE. The corresponding preprocessing, CWT, and segmentation parameters are summarized in Table A1.

A4 WAVEGUISE settings

The example wave fields differ in dimensionality, resolution, domain size, noise characteristics, and the atmospheric wave phenomena represented. Consequently, there is no single set of WAVEGUISE parameters that is optimal for all data sets. Table A1 summarizes the parameters used for the three examples presented in this study. When the CWT is applied to a data set of two spatial and one time dimension as it is done in Section 3.3 a minimum scale does not simply refer to the smallest spatial scale. Depending on the zenith angle, we find a minimum spatial scale of 2.5 km associated with stationary phase lines, i.e. a temporal scale of ∞, or a minimum temporal scale of 140 s associated with infinitely large spatial structures. A similar argument is used to explain maximum scales in the 3-D application.

https://doi.org/10.5194/egusphere-2026-5053
Preprint. Discussion started: 7 September 2026

Table A1. Summary of the preprocessing, CWT, and segmentation parameters used for the 1-D, 2-D, and 3-D WAVEGUISE examples. Definitions of the parameters are given in Sect. 2.

Parameter	1-D	2-D	3-D
Data size	72,000	700×268	$243 \times 213 \times 155$
Data resolution	30 s	2 km × 2 km	625 m × 625 m × 35 s
Noise level	0.1 hPa	0.8 BI units	80 BI units
polynomial degree	0, 1	0, 1	0, 1
Fourier components	0, 1	0, 1	0, 1
tapering	10 %	10 %	10 %
minimum scale	10 min	8 km	(2.5 km, ∞) to (∞, 2 min 20 sec)
maximum scale	25 days	268 km	(∞, 0.74 h) to (48.125 km, ∞)
dj	1/8	1/8	1/4
number of scales	86	40	17
number of azimuth angles	-	21	10
number of zenith angles	-	-	15
wavelet order	2π	2π	2π
aspect ratio	1	1	35.7
sMAD factor	-	3	-
prominence	0.01 hPa	0.2 BI units	80 BI units
connectivity	1	1	1
ε	0.088	0.123	-
retained variance	99 %	98 %	100 %

https://doi.org/10.5194/egusphere-2026-5053
Preprint. Discussion started: 7 September 2026

The retained variance quantifies the fraction of the variance of the preprocessed input wave field represented by the sum of the reconstructed wave packets and is defined as

$$R_{\mathrm{var}} = \frac{\mathrm{Var}\left(\sum_i X_i\right)}{\mathrm{Var}\left(X\right)}, \tag{A1}$$

where X denotes the preprocessed input wave field and X_i the reconstruction of wave packet i.

Author contributions. RR developed the method, carried out data analysis, and wrote the manuscript. DP provided the AWE and AMTM data and revised the manuscript. MB provided the balloon data from the Strateole-2 campaign and revised the manuscript.

Competing interests. The authors declare that they have no conflict of interest.

Acknowledgements. RR gratefully acknowledges funding from the German Research Foundation (DFG; Grant RE 5127/1-1). The AMTM operated at Río Grande was designed and built at Utah State University (USU) and the Space Dynamics Laboratory (SDL) with support from the NSF Grant 1061892. It was operated under NSF Grant 1651233. We extend our sincere thanks to the team at the Estación Astronómica Río Grande for their technical support. Finally, RR acknowledges the use of ChatGPT (OpenAI) to refine the structure and scientific tone of the manuscript.

https://doi.org/10.5194/egusphere-2026-5053
Preprint. Discussion started: 7 September 2026

References

Baumgarten, K., Gerding, M., and Lübken, F.-J.: Seasonal variation of gravity wave parameters using different filter methods with daylight lidar measurements at midlatitudes, Journal of Geophysical Research: Atmospheres, 122, 2683–2695, 2017.

Berthelemy, P. G., Wright, C. J., Hindley, N. P., Noble, P. E., and Hoffmann, L.: A novel identification method for stratospheric gravity waves in nadir viewing satellite observations, Atmospheric Chemistry and Physics, 25, 17 595–17 611, 2025.

Bramberger, M., Alexander, M. J., Davis, S., Podglajen, A., Hertzog, A., Kalnajs, L., Deshler, T., Goetz, J. D., and Khaykin, S.: First super-pressure balloon-borne fine-vertical-scale profiles in the upper TTL: Impacts of atmospheric waves on cirrus clouds and the QBO, Geophysical Research Letters, 49, e2021GL097 596, 2022.

Cao, B., Haase, J. S., Murphy, M. J., Alexander, M. J., Bramberger, M., and Hertzog, A.: Equatorial waves resolved by balloon-borne Global Navigation Satellite System radio occultation in the Strateole-2 campaign, Atmospheric Chemistry and Physics, 22, 15 379–15 402, 2022.

Chane-Ming, F., Molinaro, F., Leveau, J., Keckhut, P., and Hauchecorne, A.: Analysis of gravity waves in the tropical middle atmosphere over La Reunion Island (21 S, 55 E) with lidar using wavelet techniques, in: Annales Geophysicae, vol. 18, pp. 485–498, 2000.

Chen, C. and Chu, X.: Two-dimensional Morlet wavelet transform and its application to wave recognition methodology of automatically extracting two-dimensional wave packets from lidar observations in Antarctica, Journal of Atmospheric and Solar-Terrestrial Physics, 162, 28–47, 2017.

Corcos, M., Hertzog, A., Plougonven, R., and Podglajen, A.: Observation of gravity waves at the tropical tropopause using superpressure balloons, Journal of Geophysical Research: Atmospheres, 126, e2021JD035 165, 2021.

Corcos, M., Bramberger, M., Alexander, M. J., Hertzog, A., Liu, C., and Wright, C.: Observation of gravity waves generated by convection and the "moving mountain" mechanism during stratéole-2 campaigns and their impact on the QBO, Journal of Geophysical Research: Atmospheres, 130, e2024JD041 804, 2025.

Ehard, B., Achtert, P., Dörnbrack, A., Gisinger, S., Gumbel, J., Khaplanov, M., Rapp, M., and Wagner, J.: Combination of lidar and model data for studying deep gravity wave propagation, Monthly Weather Review, 144, 77–98, 2016.

Ern, M., Preusse, P., Alexander, M. J., and Warner, C. D.: Absolute values of gravity wave momentum flux derived from satellite data, Journal of Geophysical Research: Atmospheres, 109, 2004.

Ester, M., Kriegel, H.-P., Sander, J., Xu, X., et al.: A density-based algorithm for discovering clusters in large spatial databases with noise, in: kdd, vol. 96, pp. 226–231, 1996.

Fritts, D. C. and Alexander, M. J.: Gravity wave dynamics and effects in the middle atmosphere, Reviews of geophysics, 41, 2003.

Fritts, D. C., Pautet, P.-D., Bossert, K., Taylor, M. J., Williams, B. P., Iimura, H., Yuan, T., Mitchell, N. J., and Stober, G.: Quantifying gravity wave momentum fluxes with Mesosphere Temperature Mappers and correlative instrumentation, Journal of Geophysical Research: Atmospheres, 119, 13–583, 2014.

Fritts, D. C., Lund, T. S., Wan, K., and Liu, H.-L.: Numerical simulation of mountain waves over the southern Andes. Part II: Momentum fluxes and wave–mean-flow interactions, Journal of the Atmospheric Sciences, 78, 3069–3088, 2021.

Fritts, D. C., Stockwell, R. G., Lund, T. S., Pautet, P.-D., Sato, K., Koshin, D., Taylor, M. J., and Scherliess, L.: Initial Atmospheric Waves Experiment (AWE) imaging analyses: Gravity wave sources, temperatures, pseudomomentum fluxes, and horizontal wavenumber spectra at the OH layer, Journal of Geophysical Research: Atmospheres, 131, e2025JD045 796, 2026.

Geldenhuys, M., Kaifler, B., Preusse, P., Ungermann, J., Alexander, P., Krasauskas, L., Rhode, S., Woiwode, W., Ern, M., Rapp, M., et al.: Observations of gravity wave refraction and its causes and consequences, Journal of Geophysical Research: Atmospheres, p. e2022JD036830, 2022.

Giongo, G. A., Wrasse, C. M., Pautet, P.-D., Bageston, J. V., Nyassor, P. K., Figueiredo, C. A. O. B., Bilibio, A. V., Gobbi, D., and Takahashi, H.: A new approach to characterizing medium-scale gravity waves using Antarctic airglow observations, Atmospheric Measurement Techniques, 18, 6345–6360, 2025.

Gisinger, S., Polichtchouk, I., Dörnbrack, A., Reichert, R., Kaifler, B., Kaifler, N., Rapp, M., and Sandu, I.: Gravity-Wave-Driven Seasonal Variability of Temperature Differences Between ECMWF IFS and Rayleigh Lidar Measurements in the Lee of the Southern Andes, Journal of Geophysical Research: Atmospheres, 127, e2021JD036 270, 2022.

Haase, J., Alexander, M., Hertzog, A., Kalnajs, L., Deshler, T., Davis, S., Plougonven, R., Cocquerez, P., and Venel, S.: Around the world in 84 days, Eos, 99, 2018.

Hecht, J., Fritts, D., Wang, L., Gelinas, L., Rudy, R., Walterscheid, R. L., Taylor, M. J., Pautet, P.-D., Smith, S., and Franke, S.: Observations of the breakdown of mountain waves over the Andes Lidar Observatory at Cerro Pachon on 8/9 July 2012, Journal of Geophysical Research: Atmospheres, 123, 276–299, 2018.

Hertzog, A. and Vial, F.: A study of the dynamics of the equatorial lower stratosphere by use of ultra-long-duration balloons: 2. Gravity waves, Journal of Geophysical Research: Atmospheres, 106, 22 745–22 761, 2001.

Hindley, N. P., Smith, N. D., Wright, C. J., Rees, D. A. S., and Mitchell, N. J.: A two-dimensional Stockwell transform for gravity wave analysis of AIRS measurements, Atmospheric Measurement Techniques, 9, 2545–2565, 2016.

Hindley, N. P., Wright, C. J., Smith, N. D., Hoffmann, L., Holt, L. A., Alexander, M. J., Moffat-Griffin, T., and Mitchell, N. J.: Gravity waves in the winter stratosphere over the Southern Ocean: high-resolution satellite observations and 3-D spectral analysis, Atmospheric Chemistry and Physics, 19, 15 377–15 414, 2019.

Hirota, I. and Hirooka, T.: Normal mode Rossby waves observed in the upper stratosphere., 1984.

Kaifler, B., Kaifler, N., Rapp, M., and Dörnbrack, A.: Mountain wave momentum flux estimates from airborne lidar measurements in the middle atmosphere above the Southern Andes, Journal of Geophysical Research: Atmospheres, 130, e2025JD043 683, 2025.

Kaifler, N., Kaifler, B., Ehard, B., Gisinger, S., Dörnbrack, A., Rapp, M., Kivi, R., Kozlovsky, A., Lester, M., and Liley, B.: Observational indications of downward-propagating gravity waves in middle atmosphere lidar data, Journal of Atmospheric and Solar-Terrestrial Physics, 162, 16–27, 2017.

Krisch, I., Preusse, P., Ungermann, J., Dörnbrack, A., Eckermann, S. D., Ern, M., Friedl-Vallon, F., Kaufmann, M., Oelhaf, H., Rapp, M., et al.: First tomographic observations of gravity waves by the infrared limb imager GLORIA, Atmospheric Chemistry and Physics, 17, 14 937–14 953, 2017.

Kruse, C. G., Smith, R. B., and Eckermann, S. D.: The midlatitude lower-stratospheric mountain wave “valve layer”, Journal of the Atmospheric Sciences, 73, 5081–5100, 2016.

Lamborn, B., Scherliess, L., Ruley, L., Latvakoski, H., Syrstad, E., Sevilla, P., Zhao, Y., Cantwell, G., Taylor, M., and Pautet, P.: Atmospheric waves experiment (AWE) mission overview, in: Infrared Remote Sensing and Instrumentation XXXII, vol. 13144, pp. 274–289, SPIE, 2024.

Lehmann, C., Kim, Y.-H., Preusse, P., Chun, H.-Y., Ern, M., and Kim, S.-Y.: Consistency between Fourier transform and small-volume few-wave decomposition for spectral and spatial variability of gravity waves above a typhoon, Atmospheric Measurement Techniques, 5, 1637–1651, 2012.

https://doi.org/10.5194/egusphere-2026-5053
Preprint. Discussion started: 7 September 2026

Mixa, T., Dörnbrack, A., and Rapp, M.: Nonlinear simulations of gravity wave tunneling and breaking over Auckland Island, Journal of the Atmospheric Sciences, 78, 1567–1582, 2021.

Mixa, T. S., Fritts, D. C., Lund, T. S., and Pautet, P.-D.: Observations and Modeling of Gravity Wave-Kelvin Helmholtz Instability (GW-KHI) Interactions in the Mesosphere and Lower Thermosphere: KHI Localization and Modulation by the GW Field, 2026.

Pautet, P.-D., Taylor, M. J., Pendleton, W., Zhao, Y., Yuan, T., Esplin, R., and McLain, D.: Advanced mesospheric temperature mapper for high-latitude airglow studies, Applied optics, 53, 5934–5943, 2014.

Pautet, P.-D., Taylor, M., Fritts, D. C., Janches, D., Kaifler, N., Dörnbrack, A., and Hormaechea, J. L.: Mesospheric mountain wave activity in the lee of the Southern Andes, Journal of Geophysical Research: Atmospheres, 126, e2020JD033 268, 2021.

Pedregosa, F., Varoquaux, G., Gramfort, A., Michel, V., Thirion, B., Grisel, O., Blondel, M., Prettenhofer, P., Weiss, R., Dubourg, V., Vanderplas, J., Passos, A., Cournapeau, D., Brucher, M., Perrot, M., and Édouard Duchesnay: Scikit-learn: Machine Learning in Python, Journal of Machine Learning Research, 12, 2825–2830, http://jmlr.org/papers/v12/pedregosa11a.html, 2011.

Rauthe, M., Gerding, M., Höffner, J., and Lübken, F.-J.: Lidar temperature measurements of gravity waves over Kühlungsborn (54° N) from 1 to 105 km: A winter-summer comparison, Journal of Geophysical Research: Atmospheres, 111, 2006.

Reichert, R., Kaifler, B., Kaifler, N., Rapp, M., Pautet, P.-D., Taylor, M. J., Kozlovsky, A., Lester, M., and Kivi, R.: Retrieval of intrinsic mesospheric gravity wave parameters using lidar and airglow temperature and meteor radar wind data, Atmospheric Measurement Techniques, 12, 5997–6015, 2019.

Reichert, R., Kaifler, N., and Kaifler, B.: Limitations in wavelet analysis of non-stationary atmospheric gravity wave signatures in temperature profiles, Atmospheric Measurement Techniques, 17, 4659–4673, 2024.

Reichert, R., Pautet, P.-D., Kaifler, B., Rhode, S., Ungermann, J., Sato, K., Janches, D., and Smith, S.: Observation of mountain waves and secondary gravity waves in the mesosphere lower thermosphere above Patagonia, Journal of Geophysical Research: Atmospheres, 131, e2025JD045 172, 2026.

Salby, M. L.: Rossby normal modes in nonuniform background configurations. Part II. Equinox and solstice conditions, Journal of Atmospheric Sciences, 38, 1827–1840, 1981.

Strube, C., Preusse, P., Ern, M., and Riese, M.: Propagation paths and source distributions of resolved gravity waves in ECMWF-IFS analysis fields around the southern polar night jet, Atmospheric Chemistry and Physics, 21, 18 641–18 668, 2021.

Torrence, C. and Compo, G. P.: A practical guide to wavelet analysis, Bulletin of the American Meteorological society, 79, 61–78, 1998.

Ungermann, J. and Reichert, R.: JuWavelet–continuous wavelet transform and S transform for wave analysis, Geoscientific Model Development, 18, 8613–8626, 2025.

Vadas, S. L. and Azeem, I.: Concentric secondary gravity waves in the thermosphere and ionosphere over the continental United States on March 25–26, 2015 from deep convection, Journal of Geophysical Research: Space Physics, 126, e2020JA028 275, 2021.

Vadas, S. L., Zhao, J., Chu, X., and Becker, E.: The excitation of secondary gravity waves from local body forces: Theory and observation, Journal of Geophysical Research: Atmospheres, 123, 9296–9325, 2018.

van der Walt, S., Schönberger, J. L., Nunez-Iglesias, J., Boulogne, F., Warner, J. D., Yager, N., Gouillart, E., Yu, T., and the scikit-image contributors: scikit-image: image processing in Python, PeerJ, 2, e453, https://doi.org/10.7717/peerj.453, 2014.

Vial, F., Hertzog, A., Mechoso, C., Basdevant, C., Cocquerez, P., Dubourg, V., and Nouel, F.: A study of the dynamics of the equatorial lower stratosphere by use of ultra-long-duration balloons: 1. Planetary scales, Journal of Geophysical Research: Atmospheres, 106, 22 725–22 743, 2001.

https://doi.org/10.5194/egusphere-2026-5053
Preprint. Discussion started: 7 September 2026

Werner, R., Stebel, K., Hansen, G., Blum, U., Hoppe, U.-P., Gausa, M., and Fricke, K.-H.: Application of wavelet transformation to determine wavelengths and phase velocities of gravity waves observed by lidar measurements, Journal of Atmospheric and Solar-Terrestrial Physics, 69, 2249–2256, 2007.

Wing, R., Martic, M., Triplett, C., Hauchecorne, A., Porteneuve, J., Keckhut, P., Courcoux, Y., Yung, L., Retailleau, P., and Cocuron, D.: Gravity Wave Breaking Associated with Mesospheric Inversion Layers as Measured by the Ship-Borne BEM Monge Lidar and ICON-MIGHTI, Atmosphere, 12, 1386, 2021.

Wright, C. and Gille, J.: Detecting overlapping gravity waves using the S-Transform, Geophysical Research Letters, 40, 1850–1855, 2013.

Wright, C. J., Hindley, N. P., Hoffmann, L., Alexander, M. J., and Mitchell, N. J.: Exploring gravity wave characteristics in 3-D using a novel S-transform technique: AIRS/Aqua measurements over the Southern Andes and Drake Passage, Atmospheric Chemistry and Physics, 17, 8553–8575, 2017.

Yue, J., Hoffmann, L., and Joan Alexander, M.: Simultaneous observations of convective gravity waves from a ground-based airglow imager and the AIRS satellite experiment, Journal of Geophysical Research: Atmospheres, 118, 3178–3191, 2013.